Printable G-putty for Frequency and Rate Independent, High Performance Strain Sensors

Daniel P. O'Driscoll, Sean McMahon, James Garcia, Sonia Biccai, Cian Gabbett, Adam G. Kelly, Sebastian Barwich, Matthias Moebius, Conor S. Boland and Jonathan N. Coleman*

D.P. O'Driscoll, S. McMahon, J. Garcia, Dr. S. Biccai, Cian Gabbett, Dr. A. Kelly, Dr. S. Barwich, Professor M. Moebius, Professor J.N. Coleman - School of Physics, CRANN & AMBER Research Centres, Trinity College Dublin, Dublin 2, Ireland

Dr. C. S. Boland - Department of Physics, University of Sussex, Brighton, BN1 9RH, UK

*colemaj@tcd.ie (Jonathan N. Coleman); Tel: +353 (0) 1 8963859.

ABSTRACT: While nanocomposite electromechanical sensors are expected to display reasonable conductivity and high sensitivity, little consideration has been given to eliminating hysteresis and strain-rate/frequency dependence from their response. For example, while G-putty, a composite of graphene and polysiloxane, has very high electromechanical sensitivity, its extreme viscoelasticity renders it completely unsuitable for real sensors due to hysteretic and rate/frequency dependent effects. Here we show that G-putty can be converted to an ink and printed into patterned thin films on elastic substrates. A partial graphene-polymer phase-segregation during printing increases the thin film conductivity by $\times 10^6$ compared to bulk, while the mechanical effects of the substrate largely supress hysteresis and completely remove strain-rate- and frequency-dependence. This allows the fabrication of practical, high-gauge-factor, wearable sensors for pulse measurements as well as patterned sensors for low-signal vibration sensing.

High-performance strain sensors are often fabricated from piezoresistive materials whose electrical resistance changes as they are deformed. Such sensors are important for a number of applications with particular attention being given to soft, wearable sensors which can monitor vital signs such as pulse and breathing.[1] In recent years nanocomposites,[2] generally consisting of 1D or 2D nanomaterials embedded in polymer matrices, have proven to be versatile materials and have been utilised in a number of end applications such as gas[3], chemical[4], thermal[5] and biological [6] sensing. In addition to this, polymer nanocomposites have been heavily studied as strain sensors [7, 8, 9]. While polymers are typically processed using methods such as compression moulding, injection moulding, extrusion and thermoforming[10], polymer nanocomposites are typically prepared by solution blending, melt mixing/compounding, *in situ* polymerisation and composite self-assembly.[11] Nanocomposite formation by printing is somewhat less common.[12]

Depending on the matrix, nanocomposite materials can be very soft and so skin-mountable.[1] They also have high working strain ranges making them ideal candidates for emerging areas such as wearable sensing.[13, 14]. Although their electrical conductivity is generally not high (usually less than ~10 S/m, as a result of nanomaterial being embedded in an insulating polymer matrix),[15] they can be extremely ductile and have high sensitivity or gauge factor, G (defined by the ratio of fractional resistance change to strain, $\Delta R / R_0 = G\varepsilon$, at low-strain).[16] One recently reported nanocomposite sensing material, a graphene-polysiloxane mixture called G-putty, displayed extremely high gauge factors of up to 500, albeit at relatively low conductivities.[17]

However, nanocomposite strain sensors have a number of significant disadvantages. In particular, their viscoelasticity can introduce resistance hysteresis,[8, 13, 18] regardless of the strain considered, and render the gauge factor strongly rate-dependent.[19] These are significant problems for strain sensors which require a unique relationship between resistance and strain. A good example of this problem is found with G-putty whose extreme softness results in severe viscoplastic relaxation on straining.[8] This means that even though G-putty has an extremely high gauge factor, it cannot be used to fabricate real strain sensors. Furthermore, there is evidence to show that the high gauge factor displayed by G-putty is intrinsically linked to its low viscosity,[13] further complicating matters.

What is needed is a method to fabricate and process nanocomposite sensing materials, leading to high gauge factor and conductivity but where the hysteresis and rate-dependence have been

suppressed. Here we have developed a method to formulate G-putty-based inks which can be printed onto directly-patterned thin films on elastic substrates. Importantly, printing results in a phase segregation, leading to a graphene rich surface region with high conductivity. This in turn allows the fabrication of very thin films which display resistances which are low enough to allow the measurement of piezoresistive effects. This is important as such thin films are mechanically pinned at the substrate-film interface in a way that significantly reduces hysteresis and rate-dependence. We have fabricated such films into high-performance sensors which can be used in a number of applications, for example in biomedical sensors or mounted on bicycles as velocity and power monitors.

RESULTS AND DISCUSSION

Printing G-putty

We hypothesised that the hysteresis problems described above might be resolved by printing G-putty as thin films on elastic substrates. Then, the mechanical properties of the sensor would be dominated by that of the substrate, frustrating the viscoelastic relaxation of the G-putty. In addition, unlike other methods for depositing graphene on polymeric surfaces, for example swelling and soaking,[15, 20] printed films can be patterned which, as we show below, allows the fabrication of functional structures.

To achieve this, we used liquid-exfoliated[13, 21] graphene nanosheets with typical size of ~500 nm (figure 1a) to prepare G-putty[22] (figure 1b). The resultant putty was then ultrasonically dispersed in solvents such as butanol and chloroform. Depending on the solvent volume used, we could obtain pastes (figure 1c) or liquid inks (figure 1d) with viscosities which could be varied over >3 orders of magnitude (figure 1e). Access to such a viscosity range is important as screen printing pastes require viscosities of 1-10 Pas while inkjet printing employs inks of much lower viscosities (4-30 mPas).[13, 23] By tuning the solvent used and paste/ink concentration, we could print thin films of G-putty via spray coating, screen-printing and aerosol-jet printing[24] (figure 1f-h) onto polydimethylsiloxane (PDMS) substrates (sylgard 184). Importantly, screen- and aerosol-jet printing allow patterning during film formation. In all cases, the films appear visually uniform, while TGA measurements (figure 1i) show printed films to have graphene contents very close to that of the bulk G-putty (in this case, 15wt%). SEM measurements (figure 1j-l) show the film surfaces to be rich in nanosheets with small amounts of polymer acting as binder. This high surface concentration of graphene in a film

with an overall graphene loading of 15wt% suggests the occurrence of a partial polymer-nanosheet phase separation during deposition. To test this, we performed SEM on a cross-section of the film prepared using focused ion beam milling (figure 1m). As shown, this process involves the deposition of a protective platinum deposit to prevent sample damage. We observe a well-defined graphene-rich network directly under the Pt (i.e. at the top-surface of the film). Below this layer is almost pure PDMS. This is clear evidence of a vertical phase segregation.

This phase segregation seems to be predominately vertical, with the graphene sheets rising to the upper surface of the printed film. Conversely, the nanosheets appear to be reasonably well distributed in the lateral (horizontal) direction. Nanosheet coverage was estimated manually through evaluation of SEM images of the film surface (a representative image is shown in S24). We estimate >90% of the surface of all films to be covered by nanosheets. Interestingly, films prepared by different printing methods appear to have slightly different morphologies, with the screen-printed film appearing somewhat porous for example. In terms of uniformity, for the spray coated films, ~90-95% of the film surface consists of nanosheets with some nanosheet-free regions of size 1-2 μm observed. In the aerosol jetted films, <3% of the surface consisted of small (<0.5 μm) nanosheet-free zones. In contrast, no nanosheet-free regions were observed in the screen-printed films. The size of the nanosheet-free regions gives a rough estimate of the length-scale associated with non-uniformities in the nanosheet network. Assuming "holes" with a mean diameter of 1.5 μm contribute 5-10% of the network area, then each hole is associated with a region of network with an area of ~5μm×5μm. This implies that sections of network with areas much larger than this are relatively uniform. Even with aerosol-jet printing, the minimum achievable resolution is 10-20 μm. This analysis implies that all achievable printed structures will contain reasonably uniform networks.

We note that even though a vertical phase segregation occurs, the overall composite composition remains unchanged from bulk G-putty as described above. As a result, we continue to refer to the printed material as G-putty.

Electromechanical properties

We performed electrical measurements for a range of graphene loadings in sprayed G-putty films as well as for the bulk G-putty which had been used to prepare the inks. The resultant conductivities are plotted versus graphene volume fraction, ϕ, in figure 2a. Both data sets are

consistent with percolation theory which describes the ϕ-dependence of the conductivity:[25] $\sigma = \sigma_0(\phi - \phi_c)^n$. As shown in the panel, going from bulk to thin film, the percolation exponent, *n*, falls while σ_0 increases, behaviour which is consistent with the reduction of inter-nanosheet tunnelling resistances.[26] As a result, the sprayed G-putty displays very high conductivity, up to 300 S/m which is at least $\times 10^6$ higher than the bulk material and considerably higher than most nanocomposites.[27]. This behaviour is consistent with the phase segregation described above resulting in a graphene-rich surface region with reduced amounts of polymer separating the nanosheets. In turn, this leads to lower inter-nanosheet junction resistances and so higher composite conductivities. Such high conductivity is of great practical importance as it allows films of a given sheet resistance (e.g. for a given application) to be prepared with sprayed G-putty at much lower thickness than would be possible with the bulk material.

This high conductivity is particularly important for the development of printed, thin film, G-putty-based strain sensors. Shown in figure 2b is data for electrical resistance as function of applied tensile strain for a ~1 μm thick film of G-putty (M_f=15%) sprayed on a thin PDMS support. As observed in many nanocomposites,[16, 28] the resistance increases steadily with strain, accumulating a ×10 resistance change at 50% strain (inset). We note that $\Delta R / R_0$ scales linearly with ε up to ~25%, much higher than can be achieved with graphene-only networks,[1, 29, 30] and competitive with the best polymer-based composites (figure S20, table 21).[31] This well-defined resistance-strain relationship allows such materials to be used to sense strain. Graphs of $\Delta R/R_0$ versus increasing ε, in the low strain region, are shown in figure 2c for sprayed G-putty films with three different graphene mass fractions. Average gauge factors are plotted versus graphene mass fraction in figure 2d and show the usual[17, 32] increase with decreasing filler loading, reaching G~110 for mass fractions below 5%, considerably higher than values of ~40 demonstrated previously for graphene networks deposited via swelling and soaking.[33] We have used a new model reported by Garcia et al.[32] to compare the G vs. ϕ data for bulk and sprayed G-putty as reported in the SI. This analysis suggests the impact of strain on inter-sheet charge transfer to be particularly important in sprayed films while strain-induced changes in network structure are dominant in bulk G-putty. We find these differences to be largely attributable to the significant variations in network morphology going from bulk to spray-deposited films.

We note that this sensing behaviour of these films is very stable. As shown in figure S21, the resistance response of these sensors was very reproducible when subjected to repeated stretch-

and-release cycling (0-2% strain at 0.3 Hz). After an initial conditioning phase, the cycling response was steady with the gauge factor varying by <20% over >18,000 cycles. In addition, during cycling the films remained attached to the substrate with no delamination observed, while SEM imaging showed no apparent change in film morphology over at least 500 cycles. In addition, the sensing response was reasonably thermally stable. As shown in figure S21 after heating to 250 C for 30 mins, the cyclic response was only slightly modified with the average gauge factor reduced from 37 to 23.

It has previously been reported that strain sensors often show negative correlations between conductivity and gauge factor.[29, 32] As shown in figure 2e, this is also the case for both bulk and sprayed G-putty. However, this graph clearly highlights the differences between these systems and shows that sprayed G-putty can achieve a given G at much higher conductivity than bulk G-putty. To put these values of G in perspective, in figure 2f we reproduce literature data for 200 nanocomposite gauge factors (representing a comprehensive survey, as originally reported in a recent review[30] plotted against their ranking (from worst to best). We find the best sprayed data from figure 2d to be well within the top 10% of gauge factors. In addition, our sensors compare well to the literature data described in ref[17] in terms of their relatively low Youngs's modulus (2 MPa, determined by the substrate) and their reasonably high strain-range of 20-25% (the range of strain where the resistance-strain curve is linear, referred to in ref[17] as the working factor).

Hysteresis and rate/frequency dependence

However, as indicated above, the biggest problem with bulk G-putty sensors is not their relatively low conductivity, but the fact their extreme softness allows the graphene network to relax under strain.[17] Such relaxation can be seen in the step strain experiment shown in figure 3a where the bulk G-putty was stretched to 0.5% strain and held before stretching again to 1% strain after 900s and again held until 1800s when it was stretched again to 1.5%. While a perfectly elastic conductor would show the resistance increasing as a "staircase", the bulk-G-putty shows sharp resistance increases followed by dramatic decays as the graphene network relaxes in the ultra-soft matrix.[13] However, we find that printed thin films of G-putty show much more staircase-like behaviour, albeit with short-lived (typically <5 s for the spray coated sample) relaxation effects at step edges (figure 3 b-d). As we show below, such spikes are not observed during dynamic testing and do not appear to be a real impediment to practical strain sensing.

We propose that the suppression of dramatic relaxation effects observed in the step strain experiments is intimately related to the thinness of the printed films. The bottom surface of the film is pinned at the substrate-film interface meaning that very little relaxation is possible in the vicinity of this interface. For a thick film, relaxation would be possible in regions of composite far away from this interface. However, as film thickness is reduced, the size of this far-away zone where relaxation can occur is reduced until, for very thin films (as we have here), all of the film volume is relatively close to the substrate-film interface such that very little relaxation is possible, even at the air-film interface (i.e. the region furthest from the substrate-film interface). Under these circumstances, the film displays quasi-elastic behaviour with a mechanical response which is dominated by the substrate. Incidentally, a system like this can only act as a sensor if the resistance of such a thin film is low enough to allow electromechanically sensing. This is only the case here because the phase segregation described above results in relative high composite conductivities.

That the mechanical response of the system is dominated by the substrate is demonstrated in figure 3e. While the extreme viscoplastic response of bulk G-putty results in very large stress-strain hysteresis in bulk G-putty (figure 3e) the thin film of G-putty sprayed onto PDMS shows much more elastic-like behaviour with minimal hysteresis. One would expect the latter behaviour to allow effective practical strain sensing.

To test this, we applied and then released strain for a number of samples at various strain rates. As illustrated in figure 3f, for bulk G-putty the hysteresis is so severe that after unloading the resistance is well below the initial resistance. In contrast, for the sprayed film, although hysteresis is still present, it is greatly reduced with the resistance returning to its initial value. Having defined the hysteresis as the area of the hysteresis loop divided by the area under the R-strain curve associated with the loading cycle, we plotted the hysteresis versus strain rate for bulk G-putty as well as sprayed films in figure 3g. For bulk G-putty the hysteresis was very large and strain-rate dependent, varying from 0.25 to -1 (the sign is negative if the resistance is higher in the unload cycle compared to the load cycle). However, for the printed films, the hysteresis was much lower (~0.15) and virtually rate independent.

Such low hysteresis and rate-independence are critical for practical sensors where the relationship between resistance and stain must be similar under all circumstances. The invariance of the response of printed, thin-film G-putty can be seen by plotting the measured quasi-static gauge factor as a function of strain rate for spray-coated sensors in figure 3h with

bulk G-putty data shown for comparison. While the bulk G-putty shows very significant rate dependence, the sprayed sensor shows almost perfect rate independence.

Such rate independence suggests that the oscillatory response of printed G-putty will also be frequency independent. To test this, we applied strains oscillating between 0 and 0.5% at various frequencies to sprayed G-putty as well as bulk G-putty (see figure 3i-j). Again, while the dynamic gauge factor varied significantly with frequency for the bulk G-putty, the sprayed films showed frequency independent behaviour. (N.B. hysteresis, quasi-static G and dynamic G data for screen-printed and aerosol-jet printed films are shown in the SI).

In order to assess the performance of printed G-putty against state-of-the-art strain sensors we have compiled data (table S1), for a range of bulk and printed nanocomposite strain sensors from the literature. We note that the performance printed G-putty is highly competitive when compared to literature data across a range of metrics such as gauge factor, hysteresis and strain rate independence.

Strain sensors

We believe these properties make printed G-putty ideal for use as real electromechanical sensors. In particular, the low modulus of the PDMS support makes the sensors very soft and so wearable – making these sensors potential candidates for applications in biomedical sensing which range from measuring breathing rate[13, 34], pulse[35] and joint movement.[9, 36]To demonstrate this, we screen printed G-putty strips onto thin PDMS films (EcoFlex – a speciality, ultra-soft elastomer which has an elastic modulus (125 kPa) similar to that of human skin (~300 kPa) [37]) which were then mounted on a subject's wrist (figure 4a-b). Even in this simple arrangement, we could measure the pulse at the radial artery (figure 4 c-d) yielding a waveform with the expected profile.[15, 38] Similar results could be achieved even when printing on a commercial band-aid (figure 4e-f). These sensors can also be used in diagnostics. For example, diagnosing swallowing difficulties (dysphagia) generally requires an invasive examination which must be carried out by a specialist.[13] However, mounting printed G-putty strips on the Adam's apple allows swallowing to be monitored quantitatively, opening the way toward diagnostic applications.

Strain sensors are generally fabricated in an undulating pattern[39] to maximise sensor length (to increase the resistance change) while spatially localising the response. Shown in figure 5 a-b are examples of such sensors patterned onto extremely thin PDMS substrates by screen- and aerosol-jet-printing respectively. We note that aerosol-jet printing allows finer features while

screen-printing gives greater scalability. In addition, figure 5c-d shows printed combinations of three sensors, each at 120^o to each other. Such structures are known as rosettes and can be used to measure strain fields.[40] To demonstrate their utility for small-strain sensing, we chose a novel application: strain sensing on bicycles.

There is a significant market within the cycling community for devices to measure speed and power output. We employ printed G-putty sensors to this end, utilising the fact that peddling results in small but well-defined oscillatory strains in the bicycle frame. Using finite element analysis (see SI), we identified positions on the frame where these strains were maximised (figure 5e). Printed sensors were then mounted by sticking the PDMS substrate to the frame (figure 5f-g). The resistance output of such a sensor is shown in figure 5h and demonstrates clear oscillatory behaviour. The Fourier transform of such a trace shows the main frequency to be dominant (figure 5i). We find the peddling frequency measured in this way to match extremely well with that measured using conventional devices (figure 5j). The amplitude of the resistance trace, ΔR_{pp}, is proportional to the strain amplitude, ε_0, and so allows measurement of the power output. For any oscillator vibrating at frequency, *f*, the mean power inputted is just the average product of force and velocity. In damped, driven oscillators, the force amplitude is proportional to displacement amplitude (i.e. strain amplitude) while we associate the velocity with the strain rate, $\dot{\varepsilon} \propto f\varepsilon$. This analysis yields $\langle P \rangle \propto f\varepsilon_0^2$ and so $\langle P \rangle \propto f\left[(\Delta R_{pp}/R_0)/G\right]^2$. Shown in figure 5k is data for the measured resistance peak-to-peak amplitude (normalised to R_0) plotted versus $\langle P \rangle / f$ for both spray-cast and screen-printed sensors at various combinations of independently measured peddling frequency and power. We find a linear scaling between $\Delta R_{pp}/R_0$ and $\sqrt{\langle P \rangle / f}$, reasonably consistent with simple oscillator behaviour allowing resistance measurements to yield power output.

We can also demonstrate use of the rosette to measure the strain field in the bike frame. Finite element analysis was used to estimate the strain due to peddling in the frame along the directions of the sensors marked as 1, 2 and 3 in figure 5g. As shown in figure 5l, while the axial strain (in direction of sensor 3) is predicted to be dominant, non-zero components should exist in the direction associated with sensors 1 and 2. Shown in figure 5M are the measured resistance outputs associated with sensors 1-3 during peddling. While the axial strain (sensor 3) is indeed dominant, oscillatory strains with the correct phases and appropriate magnitudes

can be seen in the other two sensors. Using the measured gauge factors of these sensors (G≈40), we estimate the actual strain on the right axis. This shows the maximum strain in sensors 1 and 2 to be ~10^{-4} (0.01% or 100 μ-strain), a relatively small value which nicely demonstrates the sensitivity of these printed sensors.

CONCLUSION

In conclusion, we have shown that a G-putty based inks can be printed into patterned thin films with high values of both gauge factor and conductivity. The low film thickness combined with pinning at the film-substrate interface prevents relaxation under strain and supresses electromechanical hysteresis resulting in a sensing response which is independent of both strain-rate and frequency. Printed G-putty-based rosette-type sensors can measure strain fields and strains as low as ~10^{-4}.

METHODS

The viscoelastic, silicone-based material "G-putty" was formulated according to the methods previously described by the authors.[31] The material was then dispersed in a low boiling point solvent and sonicated to achieve the polymer-composite based inks described in this work. The loading level is of the inks is controlled by the loading level of the constituent G-putty. Deposition of the inks was performed using spraying, aerosol jet printing and screen printing (see SI) onto two different silicone-based elastomeric materials substrates (Sylgard 184 and EcoFlex). Both materials are two component systems consisting of a polymeric base and a curing agent which form thin, flexible elastomers when combined and cured. More detailed methods are given in the SI.

ACKNOWLEDGEMENTS: We acknowledge the European Research Council Advanced Grant (FUTURE-PRINT) and the European Union under grant agreements n°785219 Graphene Flagship-core 2. We have also received support from the Science Foundation Ireland (SFI) funded centre AMBER (SFI/12/RC/2278) and SFI 17/CDA/4704 and availed of the facilities of the SFI-funded AML and ARM labs.

AUTHOR CONTRIBUTIONS: DO'D, SMcM, JG, SB, AGK, SB, CSB and MM contributed to acquisition, analysis, or interpretation of data. DO'D, SMcM and JNC conceived and designed the work. JNC analysed data and wrote the paper.

SUPPORTING INFORMATION

The Supporting Information is available on the Wiley Publications website.

COMPETING INTERESTS: The authors declare no competing interests.

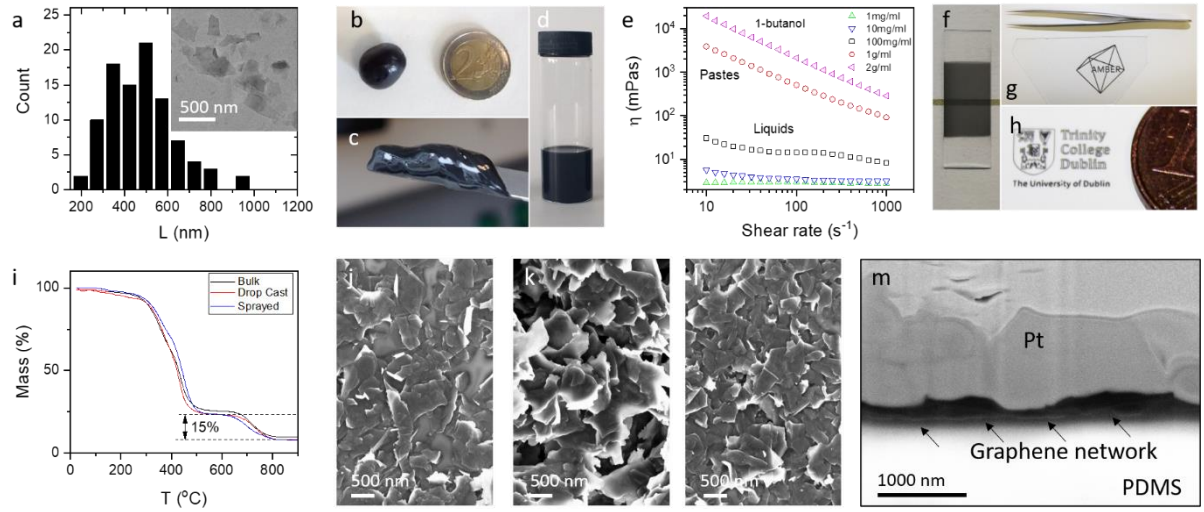

Figure 1: Formulation and printing of G-putty ink. a) TEM image of graphene used in G-putty fabrication (inset) and histogram of length of nanosheets observed in TEM images (main graph). b-d) Photographs of bulk G-putty (b), a paste of G-putty dissolved in a small amount of butanol (c) and a liquid ink prepared by dispersing bulk G-putty in chloroform (d). e) Rheology measurements for butanol-based inks at various concentrations (corresponding to G-putty mass divided by solvent volume). Note that the two highest concentration samples are pastes. f-h) Photographs of thin films of G-putty prepared by spraying (f), screen-printing (g) and aerosol-jet printing (h). i) Thermogravimetry measurements for bulk G-putty, a film of G-putty formed by drop-casting ink into a Teflon tray and a sprayed G-putty film. j-l) SEM images of the surface of G-putty films (15wt% graphene) prepared by spraying (j), screen-printing (k) and aerosol-jet printing (l). m) SEM image of a sample cross-section prepared using focused ion beam milling, showing a well-defined graphene layer (black) above a PDMS layer (white). The top Pt layer was deposited to prevent sample damage from the ion beam.

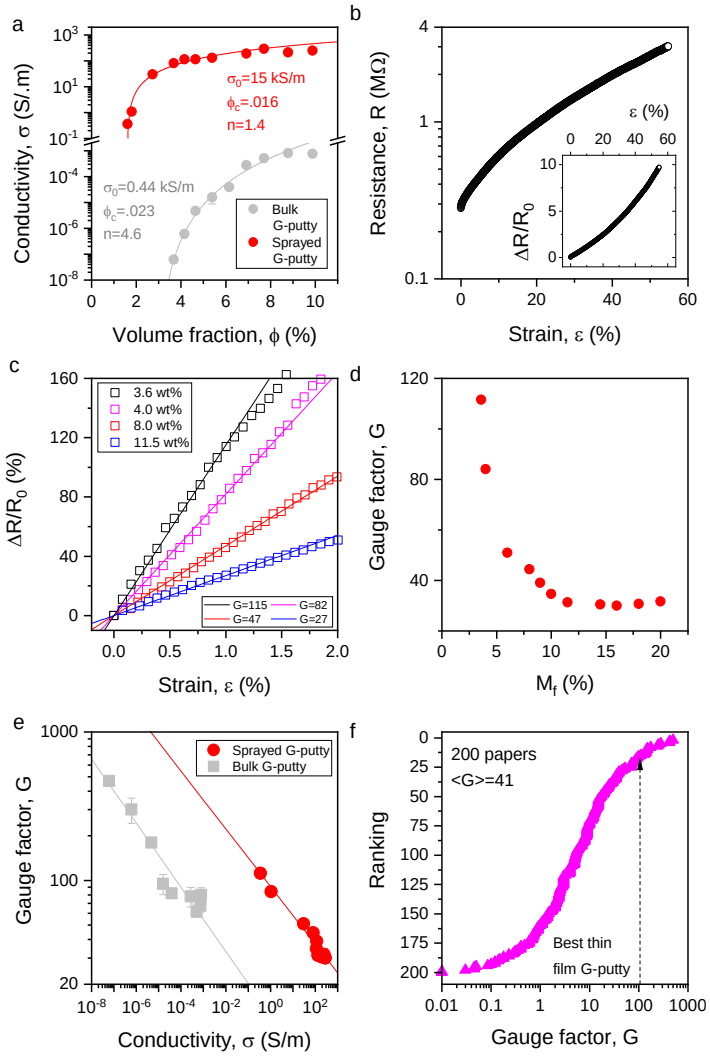

Figure 2: Electromechanical properties of sprayed G-putty films. a) Conductivity plotted as a function of graphene volume fraction for bulk and sprayed G-putty. The solid lines are fits to percolation theory with fit parameters given in the panel. b) Resistance-strain curve (inset fractional resistance change) for sprayed G-putty (M_f=15%). c) Fractional resistance change vs. strain for sprayed G-putty of four different mass fractions. d) Gauge factor versus mass fraction for spray cast G-putty. e) G vs. conductivity for both bulk and sprayed G-putty, each for various values of M_f. f) Ranking (ordered from 200 for lowest G to 1 for highest G) versus reported value of low-strain G for data extracted from 200 published papers (see ref[20]). Plotted this way, the curve approximates the cumulative distribution function[17] of the set of published G values.

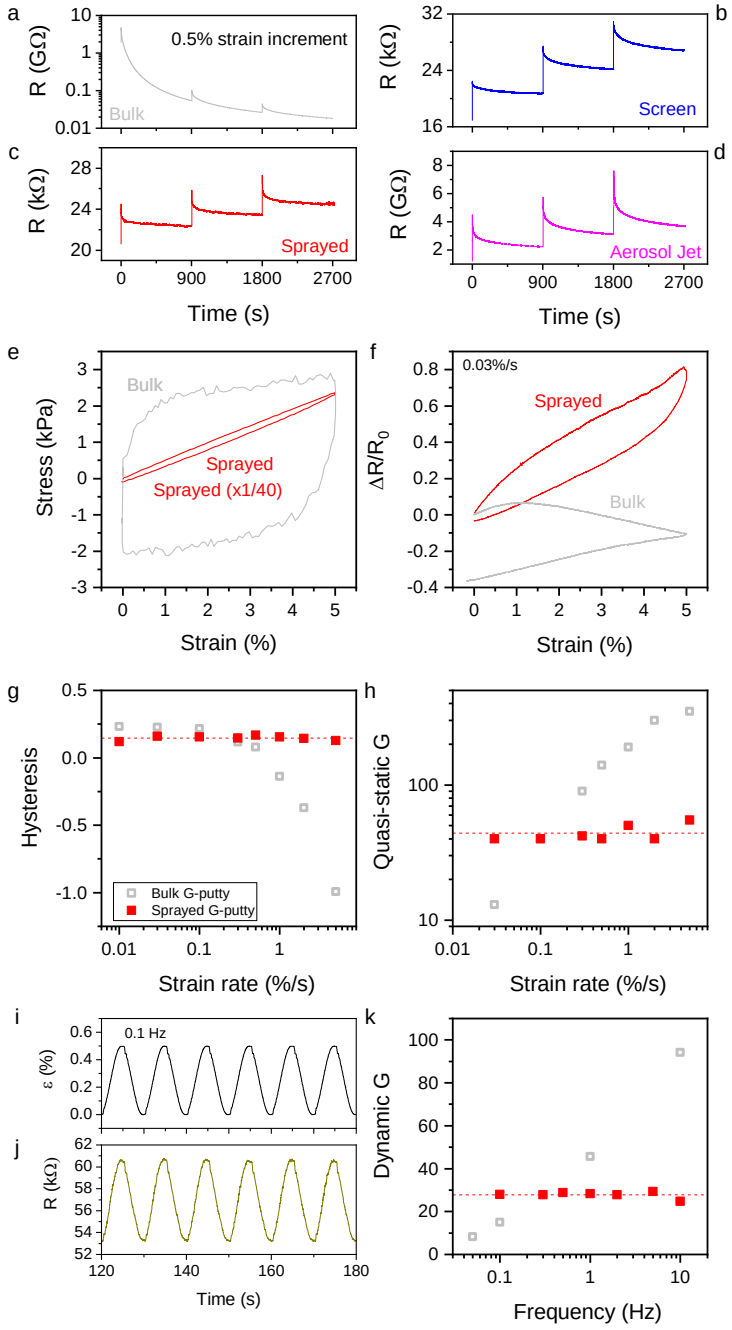

Figure 3: Time- and rate-dependent properties of G-putty. a-d) Resistance versus time for bulk (a), sprayed (b), screen-printed (c) and aerosol jet-printed (d) G-putty. In each case the sample was exposed to three successive 0.5% strain increments at 0, 900 and 1800 s. e) Stress strain curves (including strain release) for sprayed and bulk G-putty. The sprayed data set has been reduced by a factor of 40 to make it fit on the same graph as the bulk data (necessary because the mechanics of the sprayed sample is dominated by the substarte). f) Fractional resistance-change vs. strain curves (including strain release) for sprayed and bulk G-putty. g-h) Resistance hysteresis (g) and Gauge factor (h) plotted versus strain rate for bulk and sprayed G-putty. i-j) Strain (i) and resistance (j) vs. time for sprayed G-putty deformed

using sinusoidal strains at 0.1 Hz. k) Oscillatory gauge factor versus frequency for bulk and sprayed G-putty. In this graph, in all panels, red represents sprayed G-putty while grey represents bulk G-putty.

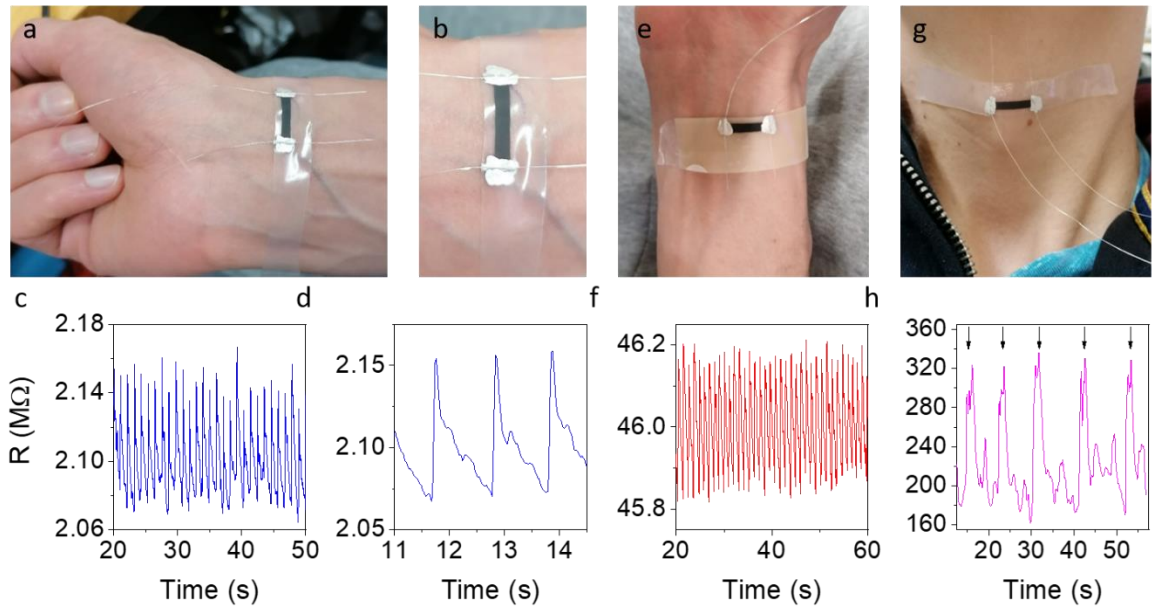

Figure 4: Applications of printed G-putty for biomedical sensing. a-d) Photographs of G-putty strips (a-b) screen printed onto an EcoFlex PDMS film and mounted on the wrist for pulse measurement (c-d). e-f) G-putty strip (e) screen printed on a commercial band-aid and mounted on the wrist for pulse measurement (f). g-h) G-putty strip screen printed onto an EcoFlex film (g) and mounted on the Adams apple of a subject to monitor swallowing (h). The swallowing events are marked by arrows. N.B. the initial resistances in c, d, f, h are different from each other because of different degrees of pre-strain applied during sensor mounting.

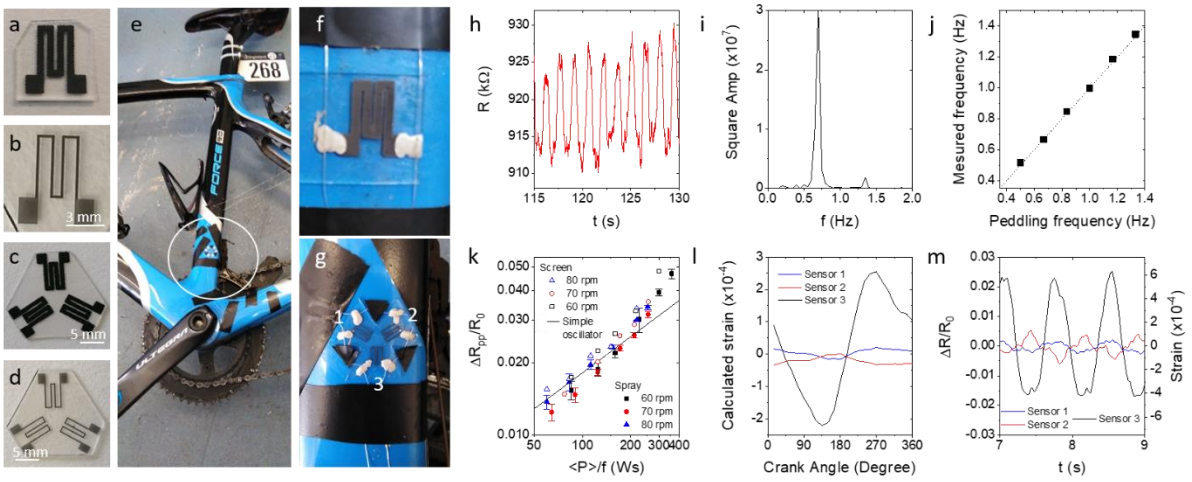

Figure 5: Application of patterned G-putty for strain sensing. a-d) Examples of printed strain sensors consisting of single gauges (a-b), printed by (a) screen- and (b) aerosol-jet printing, and rosettes (i.e. triple gauges) (c-d), printed by (c) screen- and (d) aerosol-jet printing. e-g) Photographs showing position the sensor is mounted in the bicycle frame (e) and close-ups showing single gauge (f, screen printed) and rosette (g, aerosol jet printed) sensors. h) Resistance-time trace for a screen-printed sensor mounted on a bicycle pedalled at a pedal rotation rate of 0.69 Hz. i) Fourier transform showing the pedalling frequency can be extracted unambiguously. j) Pedalling frequency measured by a G-putty sensor versus actual pedalling frequency (measured using a commercial sensor). The line represents y=x. k) Measured average peak-to-peak resistance change (normalised to strain-free-resistance) plotted as a function of peddling power divided by peddling frequency (measured using commercial sensor). Measurements were made for both a spray-cast un-patterned sensor and a screen-printed patterned sensor (G≈40 in each case), each at number of peddling powers and at three different frequencies. The line shows the scaling expected for a simple oscillator. l) Linear strain in the sensing direction calculated by finite element analysis for the three sensors shown in g as a function of crank angle. m) Resistance as a function of time measured for each of the three sensors making up the rosette in g. The right axis shows the estimated strain using G≈40.

Table of contents summary and fig

This paper describes the production of a range of graphene/polysiloxane/solvent inks which can be used to print patterned, conductive, thin films. These films have high piezoresistive gauge factors and can be used to fabricate highly sensitive strain sensors with good frequency independence and low hysteresis.

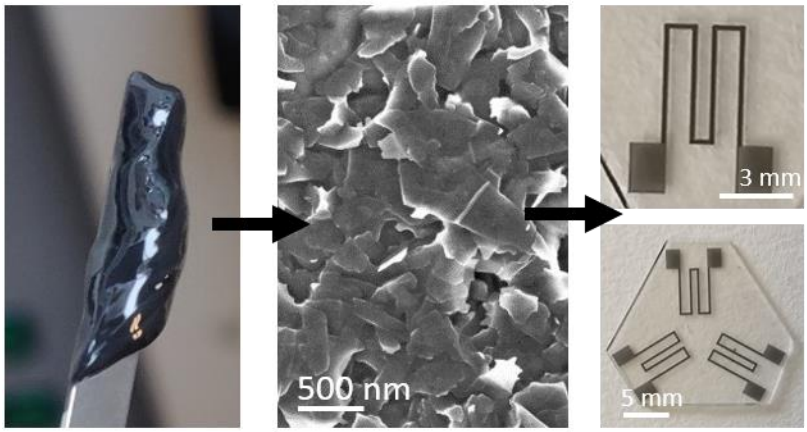

References

1. Amjadi, M.; Kyung, K.-U.; Park, I.; Sitti, M., *Advanced Functional Materials* **2016,** *26* 1678-1698.
2. Lu, Y.; Biswas, M. C.; Guo, Z.; Jeon, J. W.; Wujcik, E. K., *Biosens Bioelectron* **2019,** *123* 167-177.
3. Liu, P.; Cottrill, A. L.; Kozawa, D.; Koman, V. B.; Parviz, D.; Liu, A. T.; Yang, J.; Tran, T. Q.; Wong, M. H.; Wang, S.; Strano, M. S., *Nano Today* **2018,** *21* 18-40.
4. Yan, Y.; Yang, G.; Xu, J.-L.; Zhang, M.; Kuo, C.-C.; Wang, S.-D., *Science and Technology of Advanced Materials* **2020,** *21* 768-786.
5. Salavagione, H. J.; Diez-Pascual, A. M.; Lázaro, E.; Vera, S.; Gomez-Fatou, M. A., *Journal of Materials Chemistry A* **2014,** *2* 14289-14328.
6. Megha, R.; Ali, F. A.; Ravikiran, Y.; Ramana, C.; Kumar, A. K.; Mishra, D.; Vijayakumari, S.; Kim, D., *Inorganic Chemistry Communications* **2018,** *98* 11-28.
7. Ray, T. R.; Choi, J.; Bandodkar, A. J.; Krishnan, S.; Gutruf, P.; Tian, L.; Ghaffari, R.; Rogers, J. A., *Chemical reviews* **2019,** *119* 5461-5533; Qiu, A.; Li, P.; Yang, Z.; Yao, Y.; Lee, I.; Ma, J., *Advanced Functional Materials* **2019,** *29* 21; Zhao, J.; Zhang, G.-Y.; Shi, D.-X., *Chinese Physics B* **2013,** *22* 057701; Chun, K. Y.; Oh, Y.; Rho, J.; Ahn, J. H.; Kim, Y. J.; Choi, H. R.; Baik, S., *Nature Nanotechnology* **2010,** *5* 853-7; Shi, G.; Zhao, Z.; Pai, J.-H.; Lee, I.; Zhang, L.; Stevenson, C.; Ishara, K.; Zhang, R.; Zhu, H.; Ma, J., *Advanced Functional Materials* **2016,** *26* 7614-7625; An, H.; Habib, T.; Shah, S.; Gao, H.; Radovic, M.; Green, M. J.; Lutkenhaus, J. L., *Sci. Adv.* **2018,** *4* 0118.
8. Liu, H.; Li, Y.; Dai, K.; Zheng, G.; Liu, C.; Shen, C.; Yan, X.; Guo, J.; Guo, Z., *J. Mater. Chem. C* **2016,** *4* 157-166.
9. Wang, Y.; Wang, L.; Yang, T.; Li, X.; Zang, X.; Zhu, M.; Wang, K.; Wu, D.; Zhu, H., *Advanced Functional Materials* **2014,** *24* 4666-4670.
10. Cho, C.; Song, Y.; Allen, R.; Wallace, K. L.; Grunlan, J. C., *J. Mater. Chem. C* **2018,** *6* 2095-2104.
11. Craver, C.; Carraher, C., *Applied polymer science: 21st century*. Elsevier: **2000**.
12. Marsden, A.; Papageorgiou, D.; Vallés, C.; Liscio, A.; Palermo, V.; Bissett, M.; Young, R.; Kinloch, I., *2D Materials* **2018,** *5* 032003; Quinsaat, J. E. Q.; Burda, I.; Kramer, R.; Hafliger, D.; Nuesch, F. A.; Dascalu, M.; Opris, D. M., *Sci Rep* **2019,** *9* 13331.
13. Boland, C. S.; Khan, U.; Ryan, G.; Barwich, S.; Charifou, R.; Harvey, A.; Backes, C.; Li, Z.; Ferreira, M. S.; Mobius, M. E.; Young, R. J.; Coleman, J. N., *Science* **2016,** *354* 1257-1260.
14. Ren, J. S.; Wang, C. X.; Zhang, X.; Carey, T.; Chen, K. L.; Yin, Y. J.; Torrisi, F., *Carbon* **2017,** *111* 622-630.
15. Boland, C. S.; Khan, U.; Backes, C.; O'Neill, A.; McCauley, J.; Duane, S.; Shanker, R.; Liu, Y.; Jurewicz, I.; Dalton, A. B.; Coleman, J. N., *ACS Nano* **2014,** *8* 8819-30.
16. Bauhofer, W.; Kovacs, J. Z., *Composites Science and Technology* **2009,** *69* 1486-1498.
17. Boland, C. S., *ACS Nano* **2019,** *13* 13627-13636.
18. Lozano-Pérez, C.; Cauich-Rodríguez, J. V.; Avilés, F., *Composites Science and Technology* **2016,** *128* 25-32; Souri, H.; Banerjee, H.; Jusufi, A.; Radacsi, N.; Stokes, A. A.; Park, I.; Sitti, M.; Amjadi, M., *Advanced Intelligent Systems* **2020,** *2* 2000039.
19. Wang, T.; Ouyang, Z.; Wang, F.; Liu, Y., *SN Applied Sciences* **2020,** *2* 862; Chen, J.; Li, H.; Yu, Q.; Hu, Y.; Cui, X.; Zhu, Y.; Jiang, W., *Composites Science and Technology* **2018,** *168* 388-396.
20. O'Driscoll, D. P.; Vega-Mayoral, V.; Harley, I.; Boland, C. S.; Coleman, J. N., *2D Materials* **2018,** *5*.
21. Liscio, A.; Kouroupis-Agalou, K.; Kovtun, A.; Gebremedhn, E.; El Garah, M.; Rekab, W.; Orgiu, E.; Giorgini, L.; Samori, P.; Beljonne, D.; Palermo, V., *Chempluschem* **2017,** *82* 358-367.
22. Hernandez, Y.; Nicolosi, V.; Lotya, M.; Blighe, F. M.; Sun, Z.; De, S.; McGovern, I. T.; Holland, B.; Byrne, M.; Gun'Ko, Y. K.; Boland, J. J.; Niraj, P.; Duesberg, G.; Krishnamurthy, S.; Goodhue, R.; Hutchison, J.; Scardaci, V.; Ferrari, A. C.; Coleman, J. N., *Nature Nanotechnology* **2008,** *3* 563-8.
23. Bonaccorso, F.; Bartolotta, A.; Coleman, J. N.; Backes, C., *Advanced Materials* **2016,** *28* 6136-66.

24. Hu, G.; Kang, J.; Ng, L. W. T.; Zhu, X.; Howe, R. C. T.; Jones, C. G.; Hersam, M. C.; Hasan, T., *Chemical Society Reviews* **2018,** *47* 3265-3300.
25. Mashayekhi, M.; Winchester, L.; Evans, L.; Pease, T.; Laurila, M.-M.; Mäntysalo, M.; Ogier, S.; Terés, L.; Carrabina, J., *IEEE Transactions on Electron Devices* **2016,** *63* 1246-1253.
26. Marsden, A. J.; Papageorgiou, D. G.; Vallés, C.; Liscio, A.; Palermo, V.; Bissett, M. A.; Young, R. J.; Kinloch, I. A., *2D Materials* **2018,** *5* 19.
27. Gabbett, C.; Boland, C. S.; Harvey, A.; Vega-Mayoral, V.; Young, R. J.; Coleman, J. N., *Chemistry of Materials* **2018,** *30* 5245-5255.
28. Liu, H.; Li, Q.; Zhang, S.; Yin, R.; Liu, X.; He, Y.; Dai, K.; Shan, C.; Guo, J.; Liu, C.; Shen, C.; Wang, X.; Wang, N.; Wang, Z.; Wei, R.; Guo, Z., *J. Mater. Chem. C* **2018,** *6* 12121-12141.
29. Casiraghi, C.; Macucci, M.; Parvez, K.; Worsley, R.; Shin, Y.; Bronte, F.; Borri, C.; Paggi, M.; Fiori, G., *Carbon* **2018,** *129* 462-467.
30. Hempel, M.; Nezich, D.; Kong, J.; Hofmann, M., *Nano Letters* **2012,** *12* 5714-8.
31. Bae, S.-H.; Lee, Y.; Sharma, B. K.; Lee, H.-J.; Kim, J.-H.; Ahn, J.-H., *Carbon* **2013,** *51* 236-242.
32. Garcia, J. R.; O'Suilleabhain, D.; Kaur, H.; Coleman, J. N., *ACS Applied Nano Materials* **2021,** *10.1021/acsanm.1c00040*.
33. Hu, N.; Karube, Y.; Arai, M.; Watanabe, T.; Yan, C.; Li, Y.; Liu, Y.; Fukunaga, H., *Carbon* **2010,** *48* 680-687.
34. Yamada, T.; Hayamizu, Y.; Yamamoto, Y.; Yomogida, Y.; Izadi-Najafabadi, A.; Futaba, D. N.; Hata, K., *Nature nanotechnology* **2011,** *6* 296.
35. Gong, S.; Schwalb, W.; Wang, Y.; Chen, Y.; Tang, Y.; Si, J.; Shirinzadeh, B.; Cheng, W., *Nature communications* **2014,** *5* 1-8; Pang, C.; Lee, G.-Y.; Kim, T.-i.; Kim, S. M.; Kim, H. N.; Ahn, S.-H.; Suh, K.-Y., *Nature materials* **2012,** *11* 795-801.
36. Amjadi, M.; Pichitpajongkit, A.; Lee, S.; Ryu, S.; Park, I., *ACS Nano* **2014,** *8* 5154-5163.
37. Lu, N.; Lu, C.; Yang, S.; Rogers, J., *Advanced Functional Materials* **2012,** *22* 4044-4050; Kim, D.-H.; Lu, N.; Ma, R.; Kim, Y.-S.; Kim, R.-H.; Wang, S.; Wu, J.; Won, S. M.; Tao, H.; Islam, A., *science* **2011,** *333* 838-843.
38. Amjadi, M.; Yoon, Y. J.; Park, I., *Nanotechnology* **2015,** *26* 375501.
39. Spieker, M. R., *American Family Physician* **2000,** *61* 3639-48.
40. Park, J.; You, I.; Shin, S.; Jeong, U., *Chemphyschem* **2015,** *16* 1155-63.